

See discussions, stats, and author profiles for this publication at: <https://www.researchgate.net/publication/258456577>

Electrical and flow properties of highly heterogeneous carbonate rocks

Article in AAPG Bulletin · June 2013

DOI: 10.1306/05221312134

CITATIONS

18

READS

257

4 authors, including:



Charlotte Garing

University of Georgia

17 PUBLICATIONS 121 CITATIONS

[SEE PROFILE](#)



Linda Luquot

Spanish National Research Council

79 PUBLICATIONS 1,269 CITATIONS

[SEE PROFILE](#)



Philippe Adrien Pezard

French National Centre for Scientific Research

190 PUBLICATIONS 2,384 CITATIONS

[SEE PROFILE](#)

Some of the authors of this publication are also working on these related projects:



Deep drilling of ocean basement 1: DSDP/ODP Hole 504B (equatorial Pacific Ocean) [View project](#)



Gas Monitoring in shallow depth [View project](#)

Electrical and flow properties of highly heterogeneous carbonate rocks

Charlotte Garing, Linda Luquot, Philippe A. Pezard, and Philippe Gouze

ABSTRACT

In reservoir engineering, hydrodynamic properties can be estimated from downhole electrical data using heuristic models (e.g., Archie and Kozeny-Carman's equations) relating electrical conductivity to porosity and permeability. Although proven to be predictive for many sandstone reservoirs, the models mostly fail when applied to carbonate reservoirs that generally display extremely complex pore network structures.

In this article, we investigate the control of the three-dimensional (3-D) geometry and morphology of the pore network on the electrical and flow properties, comparing core-scale laboratory measurements and 3-D x-ray microtomography image analysis of samples from a Miocene reefal carbonate platform located in Mallorca (Spain).

The results show that micrometer- to centimeter-scale heterogeneities strongly influence the measured macroscopic physical parameters that are then used to evaluate the hydrodynamic properties of the rock, and therefore, existing models might not provide accurate descriptions because these heterogeneities occur at scales smaller than those of the integration volume of the borehole geophysical methods. However, associated with specific data processing, 3-D imagery techniques are a useful and probably unique mean to characterize the rock heterogeneity and, thus, the properties variability.

INTRODUCTION

Postdepositional hydrochemical alteration processes, including dissolution and precipitation, are controlling the development of

AUTHORS

CHARLOTTE GARING ~ *Géosciences Montpellier, Centre National de la Recherche Scientifique (CNRS), Université de Montpellier 2, 34095 Montpellier Cedex 5, France; charlotte.garing@gm.univ-montp2.fr*

Charlotte Garing is a postdoctoral researcher at the French National Center for Scientific Research in Montpellier, France. She received her Ph.D. in geosciences from the University of Montpellier in 2011. Her work focuses on field characterization and laboratory investigation of reactive transport in carbonates, using geophysical, geochemical, petrophysical, and imagery techniques. She is currently involved in CO₂ leakage remediation.

LINDA LUQUOT ~ *Géosciences Montpellier, CNRS (Centre National de la Recherche Scientifique), Université de Montpellier 2, 34095 Montpellier Cedex 5, France; linda.luquot@gmail.com*

Linda Luquot received her Ph.D. in geosciences from the University of Montpellier, France (2008). Her thesis and postdoctoral research focuses on the laboratory experiments of CO₂-rich brine injection at in-situ conditions to characterize the water-rock interactions induced by CO₂ geologic storage. She is currently working as a research scientist at the International Center for Numerical Methods in Engineering in Barcelona, Spain.

PHILIPPE A. PEZARD ~ *Géosciences Montpellier, Centre National de la Recherche Scientifique (CNRS), Université de Montpellier 2, 34095 Montpellier Cedex 5, France; ppezard@gulliver.fr*

Philippe Pezard holds a Ph.D. in earth sciences from Columbia University, New York (1990). He has been a research scientist at the French National Center for Scientific Research since 1994, now based in Montpellier, France. His research focuses on borehole geophysics, petrophysics and, recently, the development of downhole hydrogeophysical monitoring methods and instruments. He is a cofounder of imaGeau (www.imageau.eu).

PHILIPPE GOUZE ~ *Géosciences Montpellier, Centre National de la Recherche Scientifique (CNRS), Université de Montpellier 2, 34095 Montpellier Cedex 5, France; philippe.gouze@um2.fr*

Philippe Gouze received his Ph.D. in quantitative hydrology from Paris University, France (1993). In 1995, he joined the French National Center for Scientific Research, and he is currently the head

Copyright ©2014. The American Association of Petroleum Geologists. All rights reserved.

Manuscript received July 26, 2012; provisional acceptance February 27, 2013; revised manuscript received April 11, 2013; final acceptance May 22, 2013.

DOI:10.1306/05221312134

of the Transport in Porous Media Group at Geosciences Montpellier, France. His work focuses on groundwater and reservoir modeling with emphasis on reactive transport from laboratory to field scale.

ACKNOWLEDGEMENTS

Total is acknowledged for providing the funds to conduct this study. We thank Elodie Boller for her precious help in the data acquisition at the European Synchrotron Radiation Facility. We also thank the Environmental Ministry of the Government of the Balearic Islands for their support.

The AAPG Editor thanks the following reviewers for their work on this paper: Ralf J. Weger and an anonymous reviewer.

multiscale heterogeneities in carbonate rocks, leading to extremely variable and complex pore morphologies. As a result, the hydrodynamic properties may range over several orders of magnitude. For instance, more or less localized dissolution, cementation, and dolomitization events can modify irreversibly the original structure, with the formation of highly conductive zones or, at the opposite, permeability barriers. Because of the growing heterogeneity and feedback effects of the flow, transport, and reaction, virtually all types of porosity can be found within the same reservoir, depending on the local hydrogeochemical conditions. The characterization of the pore arrangements and their relations with the macroscopic properties is essential to obtain reliable parameters for reservoir exploitation or groundwater contamination models (Choquette and Pray, 1970; Chilingarian et al., 1992; Lucia, 1995; Moore, 2001; Mylroie and Carew, 2003).

The hydrodynamic properties of a reservoir are commonly estimated from electrical resistivity data using empirical resistivity-porosity and porosity-permeability relationships (Archie and Kozeny-Carman's equations). The electrical resistivity is one of the most commonly used properties to describe the morphology of a porous media. Because the electric current is predominantly conducted by the fluid phase through the connected fraction of the pore space, electrical resistivity measurements lead to valuable information about the pore network structure. Electrical resistivity has then been widely used to study the lithology, the porosity, and the water saturation of reservoirs since the pioneering works of Schlumberger (1972, 1974).

The relationship between resistivity and porosity is commonly achieved by using the empirical Archie equation (Archie, 1942):

$$F = \phi^{-m} \quad (1)$$

where ϕ and m denote the porosity and the cementation factors, respectively, and F is the formation factor, which is defined below according to Sundberg (1932) and Archie (1942):

$$F = \frac{\rho_r}{\rho_f} \quad (2)$$

where ρ_r is the resistivity of the saturated rock and ρ_f is the resistivity of the saturating fluid. Although Archie's equation has been proven to be predictive for many sandstone reservoirs, it commonly has strong limitations when applied to carbonate rocks that commonly display complex pore structures (Verwer et al., 2011). The cementation factor m , which quantifies the variation of the electrical resistivity for a given porosity, is commonly set to

2 in carbonate rocks. However, it can be extremely variable, depending on the shape and type of grains and pores, the specific surface area, or the tortuosity, for example (Salem and Chilingarian, 1999). In addition to the cementation factor, the electrical tortuosity, which is the measure of the tortuosity of the pore space affecting the mobility of electrons in a force field, is also used to link resistivity to porosity by means of empirical equations (Archie, 1942; Wyllie and Rose, 1950; Winsauer et al., 1952; Cornell and Katz, 1953; Clennell, 1997). The permeability is commonly predicted from the combination of the porosity, the critical pore size, the specific surface, the electrical resistivity, and/or the electrical tortuosity (Kozeny, 1927; Carman, 1937, 1956; Bear, 1972; Dullien, 1979). The many existing empirical relationships are commonly derived from simple models of the pore space and commonly have limitations when applied to a real media, leading to truly false permeability estimates.

This study investigates the link between porosity, electrical resistivity, and permeability by examining their relations with parameters that characterize the three-dimensional (3-D) geometry of the pore network. The overall aim is twofold: first, to propose a pertinent methodology for investigating highly heterogeneous reservoirs from pore scale to the scale at which effective macroscopic properties and parameters are commonly measured and, second, to present new data on carbonate rocks that have experienced many hydrochemical alteration events, emphasizing the control of pore structure on the petrophysical and transport properties in both cases.

The study focuses on the petrophysical properties of a Miocene reefal platform from Mallorca, Spain. The observed rocks have been submitted to various hydrological environments and chemical processes linked to saline intrusions. Repeated cycles characterized by secondary dissolution porosity, cementation features, and mineral replacement or stabilization (i.e., dolomitization and calcitization) have produced an increase in pore-size variability. In this article, we focused on zones where a rapid change of porosity has occurred. One of the zones is fully described with the characterization of the pore structure by x-ray microtomography (XRMT), which leads to 3-D images of the porous media.

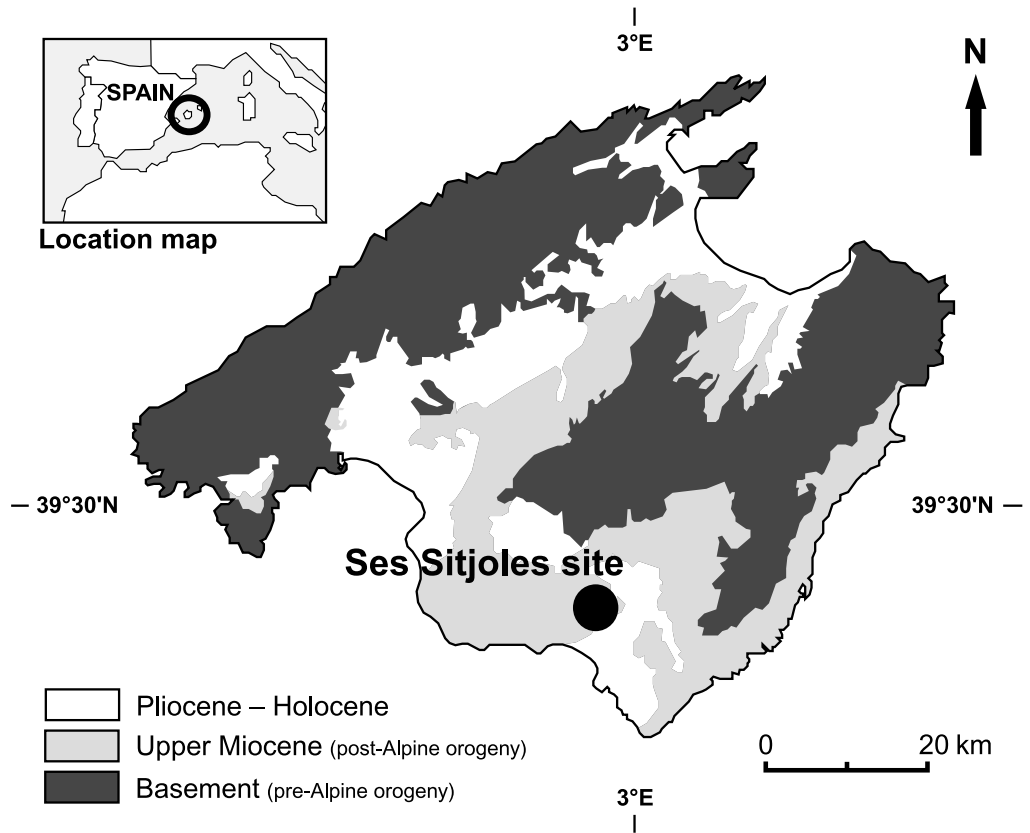
We first present electrical measurements conducted on 46 minicores (a few square centimeters each) sampled in three low-porosity zones. Then, one of these zones is investigated in great detail, including permeability measurements and original processing of 3-D XRMT data. The objective here is to study the porous network to describe the microstructure and the connectivity. The dead zones of the pore space (i.e., the part of the connected porosity that does not participate to advective transport) are mapped, and the electrical tortuosity is computed on the digital connected pore network, as well as its dominant size and specific surface.

MATERIALS AND METHODS

The Mallorca Research

The site, named the Ses Sitjoles site, has been developed since 2003 in the southeastern part of Mallorca, near the city of Campos, 6 km (4 mi) away from the coast (Figure 1), to study the salinization of the aquifer. The site (114 × 87 m [374 × 285 ft]) consists of 11 boreholes and 7 cored holes of 100-m (328-ft) depth or more. These boreholes sample a Miocene reef body with internal platform-like structures at the top, karstified reefal constructions in the middle, and forereef deposits at the base. Spectacular outcrops of the prograding Miocene reef complex, the Lluçmajor platform, are found along nearby high sea cliffs. The large-scale structure of this reef body has been extensively described (Esteban, 1979; Pomar et al., 1996; Pomar and Ward, 1999). Previous geologic and geophysical studies have been conducted on the Ses Sitjoles site and underline the heterogeneity, reactivity, and complexity of the formation (Jaeggi, 2006; Maria Sube, 2008; Garing, 2011; Hebert, 2011). This study focuses on two boreholes (MC10 and MC11) that are 2.5 m (8.2 ft) apart from each other and, more precisely, on three zones of a few centimeters and characterized by a significant change in porosity. These three zones belong to the reef barrier unit, which is highly heterogeneous because of the many dissolution and precipitation processes that have highly modified the original depositional

Figure 1. Ses Sitjoles experimental site location map.



rock fabric, resulting in indurate bioclastic calcite, vugs, molds, and cavities. The first studied zone is located in borehole MC10 between 24.8- and 25.95-m (81.4- and 85.14-ft) depth (referred as MC10-25) at the boundary between the inner platform unit and the reef barrier unit. The second one is between 37.1- and 37.2-m (121.7- and 122.0-ft) depth in borehole MC11 (MC11-37), which is close to the current water table level. The last one is located in MC10 between 61.2- and 61.7-m (200.8- and 202.4-ft) depth (MC10-61) at the boundary between the reef barrier unit and the forereef unit, which also marks the beginning of the mixing zone of fresh water and saltwater.

Petrophysical Measurements

Measurements of porosity, grain density, and electrical conductivity were conducted on 9-mm diameter and 18-mm length minicores (or plugs) sampled on the borehole cores corresponding to zones MC10-25, MC11-37, and MC10-61. The plugs were regularly cored at small intervals to fully

describe the zones and were cored perpendicular to the axis of the 9-cm (4-in.)-diameter borehole cores. The samples from zone MC10-25 depth are named with letters A to Q.

In all the cases, the porosity ϕ_{exp} and grain density ρ_{m2} were measured using the water saturation triple weighting method on dry, saturated, and immersed samples, with a precision balance of 1-mg accuracy and water prepared to be at equilibrium with the mineral. The samples were dried in an oven at 50°C for at least 3 days, and they were saturated by placing them under vacuum for 3 days before flushing them with the water and leaving them in the cell for another 2 days. The electrical conductivity of the sample σ_r was measured with two platinum electrodes and driven by a Solartron 1260 impedance meter, applying a voltage of 100 mV at a frequency of 1000 Hz to the samples saturated with a fluid of conductivity σ_f . For each sample, the measurement was conducted using four different salinities (i.e., different values of σ_f) for the saturating fluid. The formation factor F was calculated using a linear regression of σ_r plotted versus σ_f (equation 2 in terms of conductivity), and then the cementation

index m was calculated using Archie's equation (equation 1). The electrical tortuosity τ_{mes} was also deduced from the measured formation factor and porosity using the following relationship (Winsauer et al., 1952; Cornell and Katz, 1953; Clennell, 1997):

$$\tau^2 = \phi \times F \quad (3)$$

Permeability measurements were conducted on a selection of 9-mm-diameter core plugs from the zone MC10/24.8–25.95-m (81.4–85.14-ft) depth, before performing the previously listed measurements. We used a flow-through apparatus composed by two motorized piston pumps—one for the injection of rock equilibrated fluid and the other one for the back pressure control—allowing a continuous and stable percolation (fluctuations of the flow rate $Q \leq 0.01 \text{ cm}^3/\text{hr}$). Permeability k is recorded continuously by measuring the pressure drop ΔP between the inlet and outlet samples (using a differential pressure sensor Rosemount 3051) and using Darcy's law ($k = -(\mu \times L \times Q)/(S \times \Delta P)$, where μ is the fluid viscosity, and S and L are, respectively, the cross-sectional area and the length of the sample). For each sample, the permeability was recorded for at least four different flow rates and for different values of the mean pressure (ranging from 2 to 8 MPa [290–1160 psi]). More details on the equipment and the methodology used to measure the permeability can be found in Luquot and Gouze (2009).

Mercury intrusion porosimetry tests were also conducted on two of the 9-mm-diameter core plugs from the zone MC10/24.8–25.95-m (81.4–85.14-ft) depth (samples A and N), using the automated mercury porosimeter AutoPore IV 9500 V1.06 from Micromeritics Instrument Corporation. It provides not only a value of the porosity ϕ_{Hg} , such as the triple weight method, but also the mean pore entry (throat) diameter d_{Hg} .

X-Ray Computed Microtomography

X-Ray Microtomography Data Acquisition

X-ray microtomography is a noninvasive imagery technique. The 3-D image of the studied object is

computed from a set (commonly from 1000 to 2000) of two-dimensional (2-D) x-ray attenuation images. In a porous media, x-ray energy attenuation depends on the solid phase composition and the porosity. For monocrystalline rocks, XRMT maps the porosity distribution. The images are commonly displayed in normalized gray levels where black represents the voids, white represents the rock matrix, and gray levels denote the density of the microporous material scale or the microporosity.

The borehole cores (diameter, 90 mm) recovered from MC10 and MC11 were imaged using a medical-type x-ray tomography scanner (General Electrics Lightspeed) at Total-Centre Scientifique et Technique Jean F  ger, Pau, France. Longitudinal and cross section XRMT images were obtained with a pixel resolution of 190 μm horizontally (thickness) and of 625 μm vertically (spacing) along the full core length.

In addition, the 9-mm-diameter plug samples from the zone MC10-25 (samples A–Q) were imaged at the ID19 beam line of the European Synchrotron Radiation Facility in Grenoble with a pixel size of 5.06 μm . Samples A, F, K, and N were selected for advanced XRMT data processing.

X-Ray Microtomography Data Processing

Connected Porosity and Percolation Cluster

The first objective of the data processing is to identify the macroporosity. Commonly, the histogram of the gray level distribution is an overlapping bivariate distribution with a wide peak at higher attenuation coefficient values, which corresponds to voxels containing a fraction of solid phase, whereas the narrow peak at lower attenuation coefficient values corresponds to the voids. To discriminate each voxel as being either void or rock matrix, we segment the image using a growing-region algorithm (Noiriel et al., 2005). However, for some samples, one may identify three phases from the attenuation map including a microporous phase (i.e., porosity clusters formed by pores of size smaller than the pixel size). This microporous phase can be identified by performing a second segmentation step. For instance, the presence of a quasi-uniform microporous phase was visually identifiable

from the 5.06- μm -resolution images for samples F, K, and N (see discussion below). This phase was confirmed by the analysis of higher resolution XRMT images (0.42- μm pixel size) using 2-mm-diameter plugs cored near the 9-mm-diameter plugs and by scanning electron microscope images on cross sections. Sample A displays only macroporosity. We define $\phi_M^{(\text{tot})}$ the total macroporosity (i.e., the fraction of voids) that includes the pore of the diameter larger than the imagery resolution and $\varphi_\mu^{(\text{tot})}$ the total microporosity, which is given by the product of the mean intrinsic porosity $\phi'_\mu^{(\text{tot})}$, that is, the porosity of the microporous phase itself, and the fraction of the microporous phase in the sample $\varphi_\mu^{(\text{tot})}$. Finally, the total porosity of the sample is

$$\phi^{(\text{tot})} = \phi_M^{(\text{tot})} + \varphi_\mu^{(\text{tot})}\phi'_\mu^{(\text{tot})} \quad (5)$$

The mean porosity of the microporous phase $\phi'_\mu^{(\text{tot})}$ is estimated from the gray level value average over the microporous phase (noted $\langle \cdot \rangle$):

$$\phi'_\mu^{(\text{tot})} = \langle G(x) / (\langle G_v \rangle - \langle G_m \rangle) \rangle \quad (6)$$

where $G(x)$, $\langle G_v \rangle$, and $\langle G_m \rangle$, denote the gray level value at position x in the microporous phase, the sample average gray level value characterizing the void phase, and the sample average gray level defining the matrix. To compare the calculated porosity with the one measured in laboratory ϕ_{exp} , the fraction of the connected porosity should be calculated because the triple weighting method leads to a value of the porosity accessible by the saturating water. We used a cluster-labeling algorithm (e.g., Stauffer and Aharony, 1994) for identifying the networks of pore voxels that are connected with the sample boundaries. Here, we consider the percolating clusters, or sample-spanning clusters, as the clusters of porosity that are connected to the top and bottom boundaries of the sample. For high-porosity rocks such as those studied in this article, the percolation pore network is commonly formed by only one percolating cluster. In the case where a microporous phase is identified, the connected cluster analysis is also conducted on the union of the macroporosity and the microporous phase fraction. For comparing

the porosity calculated from XRMT images to the measured porosity, one has to add the porosity of the clusters that have at least one connection to any of the boundaries. At the end of this calculation procedure, one obtains the connected macroporosity ϕ_M , the connected microporosity ϕ_μ , the fraction of the connected microporous phase φ_μ , the mean intrinsic porosity of the connected microporous phase ϕ'_μ (calculated in the same way as equation 6, but considering this time the connected microporous phase), and the overall connected porosity $\phi = \phi_M + \varphi_\mu \times \phi'_\mu$. Finally, $\phi^{(\text{tot})} - \phi$ denotes the nonconnected or trapped porosity.

Mobile Versus Immobile Fraction of the Percolating Cluster

Dead-end pore structures are diffusion-dominated zones (immobile porosity) and therefore have negligible contribution to advective transport. The identification of the mobile and immobile parts of the percolating cluster can be efficiently evaluated using an algorithm described in Gouze et al. (2008). From these calculations, one can define the immobile connected porosity $\phi^{(\text{im})}$ and the mobile connected porosity $\phi^{(\text{m})}$, with the definition $\phi = \phi^{(\text{im})} + \phi^{(\text{m})}$. Commonly, such calculations that require large CPU and memory are performed for a subvolume of the full sample considered as a representative elementary volume (REV) of the sample. This step was performed on samples A and N with a subvolume of 510^3 voxels (cubic subsample). Calculations were also conducted on some larger cylindrical subvolumes: cylinder of diameter corresponding to the entire diameter of the sample (9 mm or 1779-voxel unit diameter) and length of 600 voxel units for verifying the assumption about the representativeness of the 510^3 -voxel unit subvolume.

Electrical Tortuosity Calculation from X-Ray

Microtomography Images

Assuming that the matrix is highly resistive compared to the pore-saturating fluid, the component of the effective conductivity of a cylindrical sample of length L and diameter D along axis x_i (the axis aligned with the main electrical potential) is defined through the average constitutive relation

$$\langle I(x) \rangle_{x_i} = S\sigma \langle E(x) \rangle_{x_i} \quad (7)$$

where $\langle \cdot \rangle_x$ denotes the sample-size average, I is the current density, $S = \pi D^2 / 4$ the area of the sample ends, and $E(x)$ is the electrical field: $\langle E(x) \rangle_{x_i} = -\langle \nabla V(x) \rangle_{x_i} = \Delta V / L$ with $\langle \nabla V(x) \rangle_{x_i}$ as the average gradient of potential and $\Delta V = V_{x_i=L} - V_{x_i=0}$ ($V_{x_i=L} > V_{x_i=0}$) as the potential difference. The electrical conductivity problem is described by the disordered Laplace equation:

$$\nabla \times (\sigma(x) \nabla V(x)) = 0 \quad (8)$$

where $\sigma(x)$ is the conductivity of the material that fills the connected cluster at position x . By definition $\sigma(x) = \sigma_f$ in the voxels forming the (connected) macroporosity, and we assume that $\phi(x) = \phi'_\mu \sigma_f$ in the microporous phase. Boundary conditions associated with equation 8 are fixed electrical potential at $x_i = 0$ and $x_i = L$ and null potential gradient at the fluid-solid interface. The computed electrical tortuosity (noted τ_{XRMT}) is then obtained by equations 1 and 3, where σ_r is given by equation 7 and where $\langle E(x) \rangle_{x_i}$ is obtained by solving equation 8 using here the time domain random walk approach (Dentz et al., 2012) computed on the connected cluster with or without the immobile domain.

Microstructural Descriptor Calculations from X-Ray Microtomography Images

A better description of the geometry and topology of the pore space (macroporosity) can be achieved using morphological quantities that can be extracted from the digitized images. Here, we focus on the pore-size distribution functions (pdf) (Coker and Torquato, 1995) and surface-to-volume ratio (named the specific surface) that can be easily measured from the XRMT images.

The inscribed-radii distribution function $P(x)$ gives the probability that a random point in the pore phase lies at a distance x and $x + dx$ from the nearest point on the pore-solid interface. It is achieved for each point (voxel) of the pore phase by finding the largest sphere centered on the point and that just touches the pore phase and recording its radius (Euclidean distance between the point of interest and the one on the interface pore solid). The spheres that are fully included in the bigger ones are not

considered. The algorithm used is a modified version of the one described in Meijster et al. (2000). As already mentioned, the pore structure of the studied carbonates is complex, and the conventional definition of pore and throat commonly established for the first-order characterization of sandstones seems to be inappropriate. Conversely, we propose to evaluate the dominant pore size d_{DOM} as the pore diameter corresponding to 50% porosity contribution, that is, the maximum size of pores needed to occupy half of the pore space.

RESULTS

Longitudinal XRMT images of the three studied zones, with two cross section images taken at the top and at the bottom of each zone, are presented in Figure 2. The significant change in porosity occurring over only a few centimeters is clearly visible for each zone. The porosity increases from approximately 4% to 30% over 20 cm (8 in.) of the core, with a particularly abrupt transition in the case of MC11-37.

According to Figure 3A, each zone can be described by Archie's equation (2) with mean values for the cementation index m of 2.05, 2.1, and 2.6 for MC10-61, MC11-37, and MC10-25, respectively. However, the samples with the lowest porosities deviate slightly from the linear relationship reasonably followed by the samples with porosity above 10%. Figure 3B presents the same data but was displayed depending on the pore type: the samples presenting an intergranular porosity have cementation factor m values of approximately 2, and the most vuggy samples have the highest values of m . The electrical tortuosity is approximately 2 at 30% of porosity (Figure 3C) and increases to maximum values of 9.8, 4.8, and 5.3 for, respectively, MC10-25, MC11-37, and MC10-61, which are achieved approximately 7% of porosity for MC10-25 and MC11-37 and approximately 5% of porosity for MC10-61. The values are a bit lower for the less porous samples. As for the formation factor, the samples presenting the highest tortuosity are the vuggiest samples (Figure 3D). However, samples with similar porosity and pore type

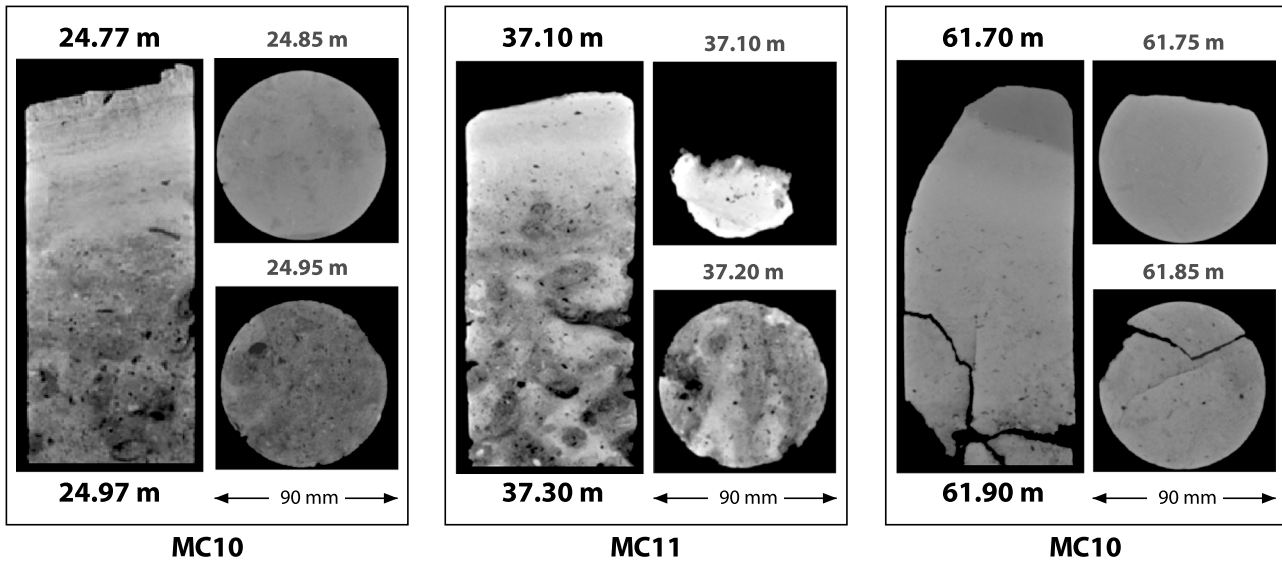


Figure 2. X-ray microtomography longitudinal and cross section images (resolution of 190 μm horizontally and 625 μm vertically) of the three low-porosity zones: MC10-25 (24.78–24.95-m [81.30–81.86-ft] depth), MC11-37 (37.1–37.2-m [121.7–122.0-ft] depth), and MC10-61 (61.7–61.9-m [1186.7–202.43-ft] depth).

can present different values of formation factor and tortuosity. The zone MC10-25 was selected for a more detailed study of the pore structure.

The evolution of the petrophysical properties of MC10-25 with depth are presented in Figure 4. The data highlight two different zones within this zone: the top, from 24.78- to 24.85-m (81.30–81.53-ft) depth (black dots), and the bottom, from 24.85- to 24.96-m (81.53–81.89-ft) depth (gray dots). The porosity ϕ_{exp} decreases from 14.9% to 4.8% in the top part and then increases again to 40% in the bottom part, which corresponds to the average value for the porosity above and below the entire zone. The values of porosity determined from mercury intrusion porosimetry (ϕ_{Hg}) for samples A and N are similar to ϕ_{exp} . The top of the zone is partially dolomitized, with a maximum value of 50% dolomite for sample G. The dolomite content decreases with depth in the bottom part, and the last samples of the zone are pure calcite. The formation factor increases and then decreases as the porosity decreases and increases. The values are, however, much higher in the top part, with an average value of 795 and a maximum value of 1834 for sample F, than in the bottom part, where the average value is 80. The cementation index decreases with depth throughout the entire zone from 2.8 to 2.4. The tortuosity

exhibits higher values in the top part than in the bottom part, with average values of 7.7 and 3.5, respectively. The maximum value is reached for sample E, which is not the tightest sample. The permeability k is approximately 8.10^{-14} m^2 ($8.61.10^{-13} \text{ ft}^2$) (80 md) in the top of the zone and then drops to values of 2.10^{-18} m^2 ($2.15.10^{-17} \text{ ft}^2$) (2 μd) or below the detection limits for the tightest samples and then increases to values of approximately 4.10^{-15} m^2 ($4.31.10^{-14} \text{ ft}^2$) (4 md) in the bottom zone.

X-ray microtomography images are available for these samples, apart from E and H. The examination of the raw data indicates that the pore structure is similar for A, B, C, and D; for F and G; for I, J, K, and L; and for M, N, O, P, and Q. The data were then analyzed for one sample of each group: A, F, K, and N. Sample A was segmented into two phases: the solid rock matrix (in white) and the macroporosity (in black), and samples F, K, and N were segmented into three phases—the solid rock matrix (in white), the macroporosity (in black), and the microporous phase (in red)—which consist of microporous matrix with pores smaller than 5.06 μm . An example of a slice after segmentation is shown for each sample in Figure 5. In the top zone of MC10-25, represented by sample A, the pore structure consists of vugs within a compact matrix. With depth, less and less pores are

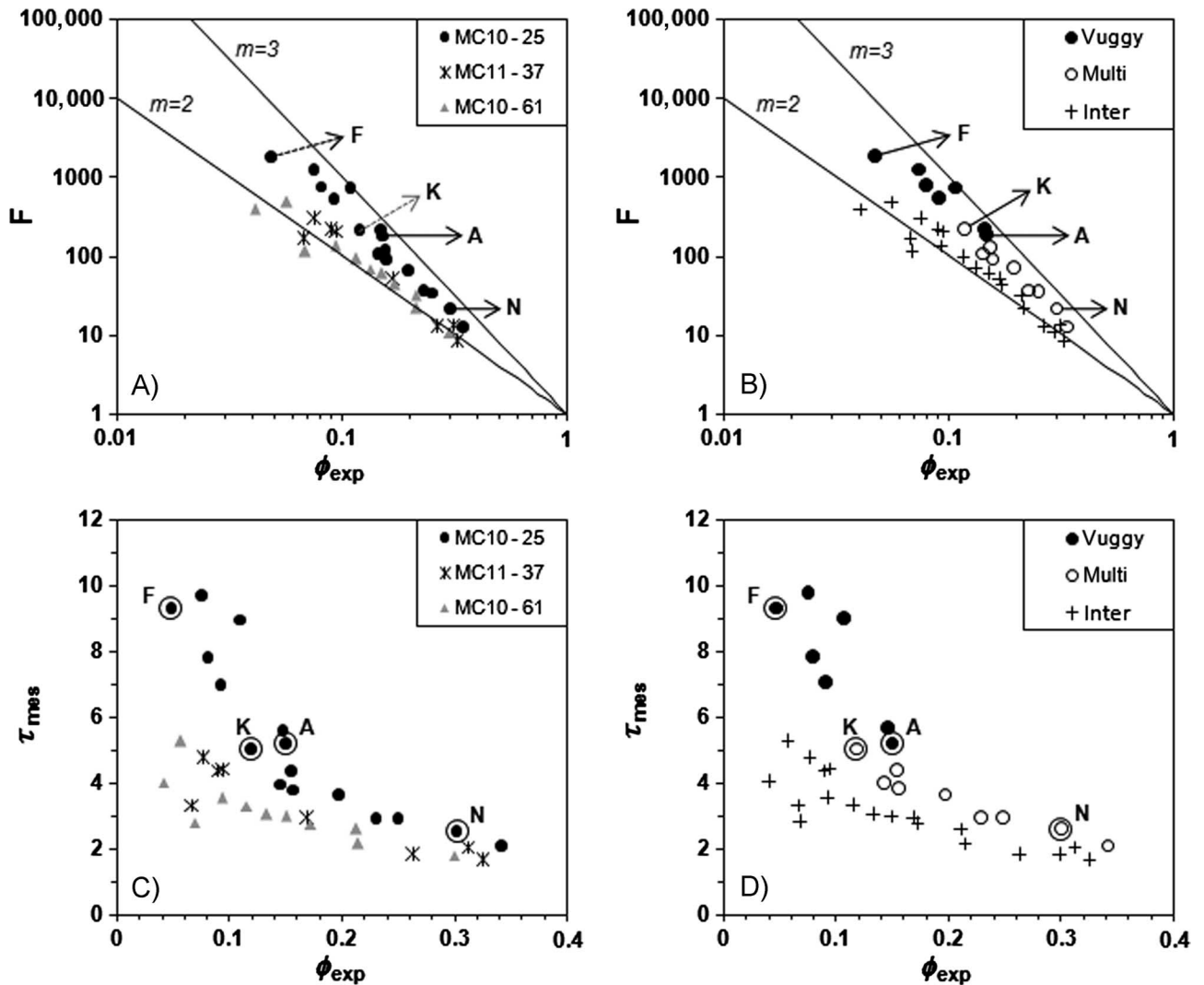


Figure 3. Crossplots of formation factor F and tortuosity τ_{mes} versus porosity ϕ_{exp} depending on the zone (graphs A and C) and depending on the porosity type (graphs B and D). In graphs A and B, lines of equal cementation factor (m) according to Archie's equation are also shown. In graphs B and D, "multi" stands for samples presenting multiple porosity types (intergranular, moldic, and vuggy) and "inter" stands for intergranular porosity.

observed, and the size of the pores becomes smaller and the matrix becomes microporous, as can be seen in sample F. Between F and K, the size of the pores does not seem to change, but more pores exist, and so the porosity is higher in sample K, with a high proportion of microporosity. In sample N, pores are a bit larger and more numerous, the matrix is still microporous, and many bioclasts are observed.

The fractions of the macroporous and microporous phases were calculated for the entire scanned samples, and then the percolating clusters were established to study the connectivity of the porosity. Sample A has a total porosity of 18.2%, which

consists of the total macroporosity only. One percolating cluster giving a z direction connected porosity of 14.7% exists. When including pores connected to at least one boundary, the final connected porosity is 14.9% (82.1% of the macroporosity), which is similar to the porosity measured in the laboratory. Samples F, K, and N have both macroporosity and microporosity phases, with respective proportions of 44.8% and 55.2% for sample F, 33.5% and 66.5% for sample K, and 33.7% and 66.3% for sample N. For all these samples, no percolating clusters were found for the macroporosity phase. For samples N and K,

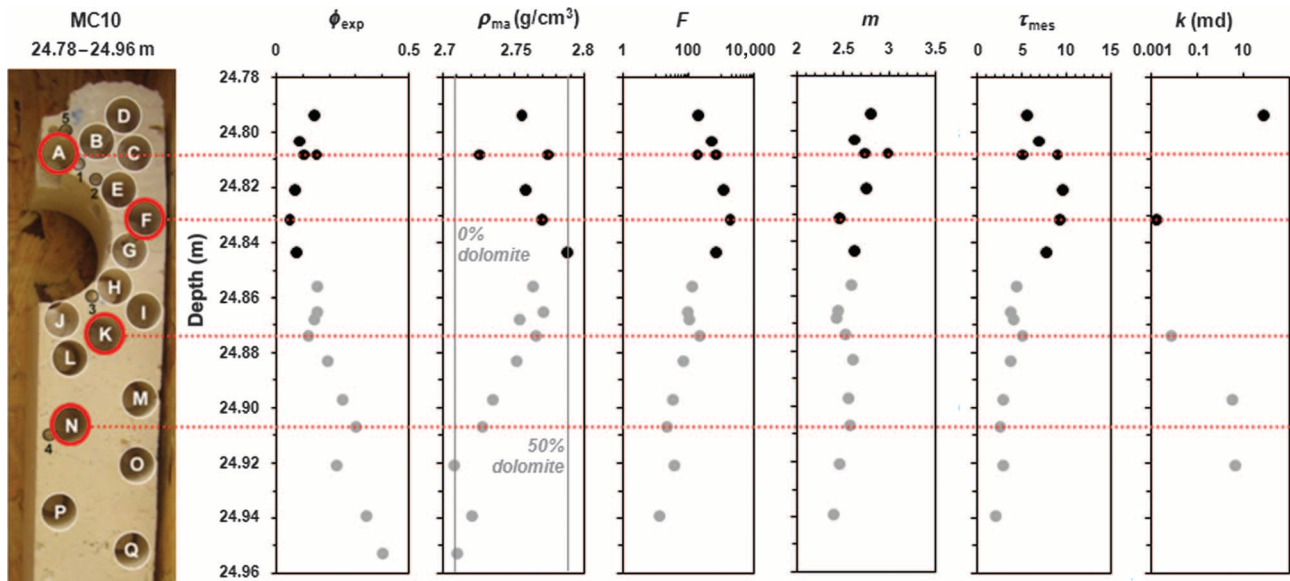


Figure 4. Variation with depth of the measured petrophysical parameters at MC10-25. The plug location is given on the photograph (left). This studied part of the reservoir can be separated into a top zone (black dots) and a bottom zone (gray points).

the union of the macroporosity and the microporous phase form for each sample a connected cluster in the z direction. Conversely, the union of the macroporosity and the microporous phase in sample F does not even make a z direction connected cluster, whereas a porosity of 4.8% was measured in the laboratory. For sample K, the percolating cluster formed by the union of the macroporosity and the microporous phase represents a volume fraction of 4.3%, much lower than the experimental value of the connected porosity (11.9%). Finally, sample N has one percolating cluster formed by the union of the macroporosity and the microporous phase, which represents a volume fraction of 32.8%, with

11.4% of macroporosity (ϕ_M) and 21.4% of microporous phase (ϕ_μ). The porosity of the microporous phase ϕ'_μ estimated from the gray levels is 86%. With $\phi_M = 11.4\%$ and $\phi_\mu = \phi_\mu \times \phi'_\mu = 18.4\%$, we obtain a total connected porosity of 29.8%, which is similar to the experimental connected porosity.

The results for A and N are summarized in Figure 6A. The experimental data of porosity (ϕ_{exp}) also displayed on the same graph are in good agreement with the computed connected porosity for both samples. Figure 6B displays the results from mercury injection tests conducted on samples A and N. The curves of the cumulative intrusion versus pore diameter confirm the macroporous

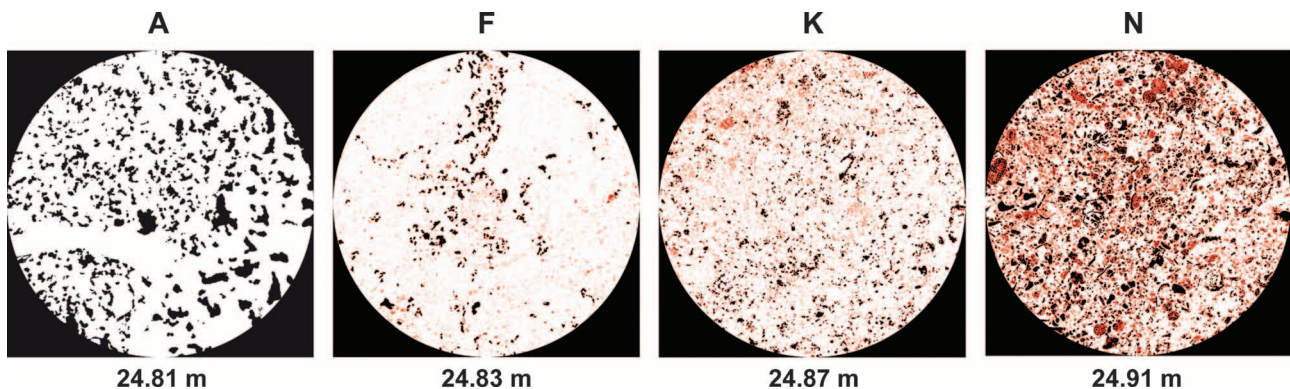


Figure 5. Numerical cross section (slice) through the three-dimensional x-ray microtomography images for samples A, F, K, and N. Pixel size is $5.06 \mu\text{m}$ (white = rock matrix; black = macroporosity; red = microporosity).

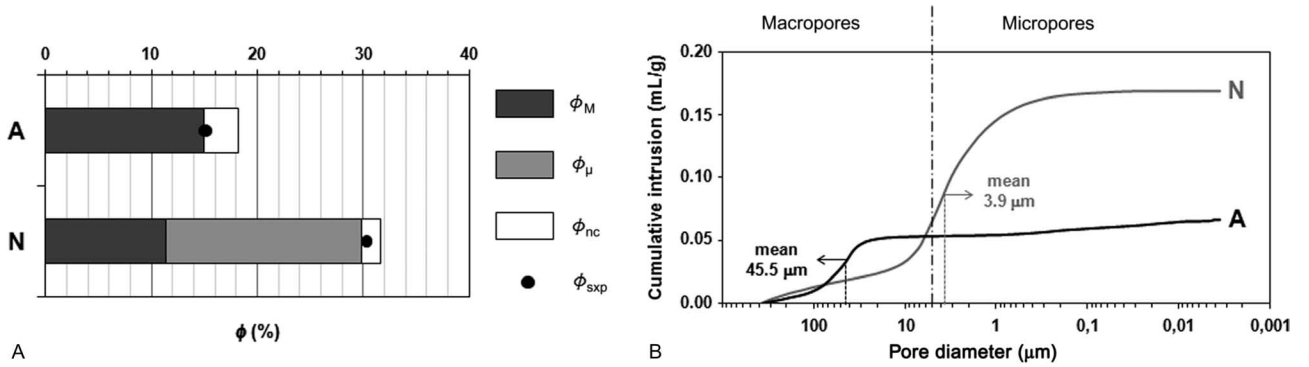


Figure 6. (A) Connected macroporosity (ϕ_M), connected microporosity (ϕ_μ), and nonconnected macroporosity and microporosity (ϕ_{nc}) computed from the x-ray microtomography images for samples A and N, and comparison with the value of the porosity measured in the laboratory with the triple weight method (ϕ_{exp}). (B) Pore-entry size distribution determined with mercury injection tests on samples A and N.

nature of the pore space of sample A and the presence of a high fraction of microporosity in sample N. Sample A has a mean pore-throat diameter d_{Hg} of 45.5 μm . Sample N has a much smaller d_{Hg} of 3.9 μm , which is below the resolution of the XRMT and corresponds to the microporosity. An example of how the microporosity clusters (in gray) act to connect macroporosity clusters (in black) in sample N is shown in Figure 7.

The evaluation of the mobile and immobile domains was conducted on a cube of 510^3 voxels (cubic subsample) considered as a REV for the connected macroporosity of sample A and for the connected macroporosity plus microporosity of sample N. Figure 8 displays for both samples a 3-D representation of the entire connected porosity and the 3-D images of the mobile (blue) and immobile (red) domains for the REV with two examples of cross sections. The black voxels on the 2-D representation stands for the unconnected porosity, and the light gray is the solid rock matrix. Sample A contains a high fraction of immobile zones, representing 65% of the connected porosity, whereas the immobile domain accounts for 14% of the connected porosity in the case of sample N. The values of porosity computed before and after the removal of the immobile domain on the cubic subsample ($\phi_{XRMT}^{(cube)}$) are presented in Table 1. The value of porosity computed on the REV before removing the immobile domain is similar to the value of porosity computed on the total sample ($\phi_{XRMT}^{(full)}$) in the case of sample N, but not in the case of sample A.

For this last sample, this step was then conducted on a bigger subsample, corresponding to a cylinder of a diameter equal to the diameter of the total sample and a length of 600 voxels (cylindrical subsample). The value of porosity computed on this subsample ($\phi_{XRMT}^{(cylinder)}$) with the immobile domain is similar to the porosity of the total sample, and the percentage of immobile zone in that case is 57%.

The electrical tortuosity computed on the cubic and cylindrical subsamples before and after the removal of the immobile domain is also displayed in Table 1, together with the measured tortuosity. The tortuosity computed on the subsamples ($\tau_{XRMT}^{(cube)}$ and $\tau_{XRMT}^{(cylinder)}$ for sample A and $\tau_{XRMT}^{(cube)}$ for sample N) are higher and closer to the measured values (τ_{mes}) when the immobile domain is considered, especially in the case of sample A because it contains a

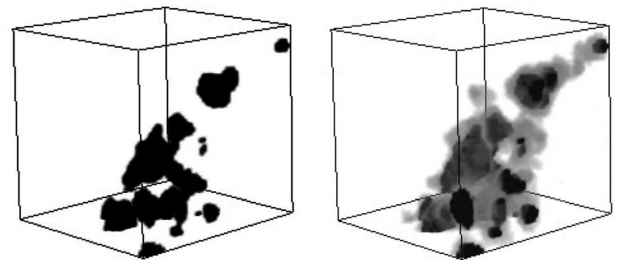


Figure 7. Connection of the macroporosity by the microporosity in sample N on a cube of $50 \times 50 \times 50$ pixels. The image on the left shows the macroporosity alone (in black), and the image on the right shows the union of the macroporosity and the microporosity (in gray), which creates a connected cluster.

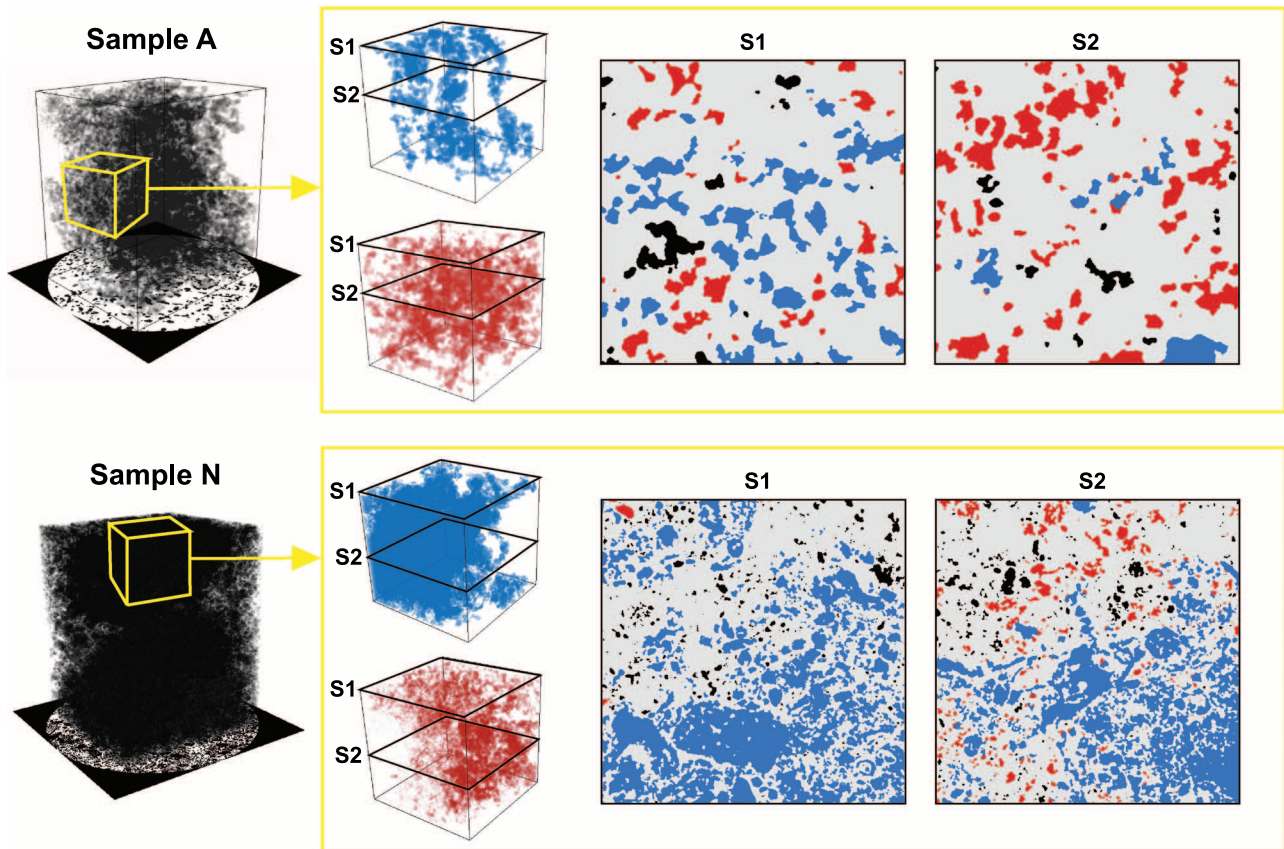


Figure 8. Three-dimensional representation of the percolating cluster for the macroporosity sample (A) and the macroporosity + microporosity sample (N). Three-dimensional images of the mobile (blue) and immobile (red) fraction of the connected cluster on the cubic subsample (yellow cube) with two cross sections, S1 and S2, displayed as an example. The unconnected porosity appears in black in the cross sections.

high proportion of immobile zones, and for the cylindrical subsample, which, as seen before, is more representative of the total sample than the cubic subsample.

The calculation of the pore size and the specific surface were conducted on the connected network

for samples A and N. Sample A exhibits pores with a maximum diameter d_{MAX} of 525 μm and a dominant pore-size diameter d_{DOM} of 84 μm . Sample N also contains macropores that can reach almost 500 μm of diameter with a lower d_{DOM} (50 μm), but the microporosity envelope, which connects

Table 1. Values of the Porosity of the Percolating Cluster Computed on the Entire Sample $\phi_{XRMT}^{(full)}$ and Values of Porosity and Tortuosity Computed on the Cubic Subsample $\phi_{XRMT}^{(cube)}$ and $\tau_{XRMT}^{(cube)}$, for Samples A and N and Also on the Cylindrical Subsample $\phi_{XRMT}^{(cylinder)}$ and $\tau_{XRMT}^{(cylinder)}$ in the Case of Sample A*

		Full Sample			Cubic Subsample		Cylindrical Subsample	
		ϕ_{exp}	τ_{mes}	$\phi_{XRMT}^{(full)}$	$\phi_{XRMT}^{(cube)}$	$\tau_{XRMT}^{(cube)}$	$\phi_{XRMT}^{(cylinder)}$	$\tau_{XRMT}^{(cylinder)}$
Sample A	With immobile domain	0.149	5.23	0.147	0.17	6.52	0.141	5.24
	Without immobile domain	0.149	5.23		0.058	2.11	0.06	1.65
Sample N	With immobile domain	0.301	2.57	0.285	0.282	2.59		
	Without immobile domain	0.301	2.57		0.241	2.33		

*The data computed on the subsamples are given before and after the removal of the immobile domain, and the values of the experimental tortuosity τ_{mes} are added for comparison.

Table 2. Summary of the Petrophysical Properties and the Connectivity of the Porous Network for Samples A, F, K, and N, and the Characteristics of the Connected Network for Samples A and N

		A	F	K	N
Petrophysical results	ϕ_{exp}	0.149	0.047	0.119	0.301
	F	183	1834	216	21
	m	2.74	2.47	2.52	2.57
	τ_{mes}	5.23	9.35	5.07	2.57
	k	80 md	0.002 md	0.007 md	4 md
	d_{Hg}	45 μm	–	–	3.9 μm
Connectivity		Macropores (>5 μm)	No percolation clusters found (micropores [$\leq 5 \mu\text{m}$] smaller than the resolution of the images)		Macropores connected by micropores only
		Connected network of 82%			Connected network of 95%
Characteristics of the percolating network		65% immobile zones			14% immobile zones
	ϕ_{XRMT}	14.7			29.9
	τ_{XRMT}	5.24			2.59
	d_{DOM}	84 μm			16.5 μm
	S/V	8.4 mm^{-1}			57 mm^{-1}

the macropores of sample N, has a much lower d_{DOM} (16 μm), with no diameter exceeding 90 μm . The connected macroporosity of sample A has a specific surface, S/V , of 8.4 m^{-1} (2.6 ft^{-1}). For sample N, the specific surface of the macroporous phase of the connected network is higher, with a value of 19 m^{-1} (5.8 ft^{-1}), and so is the one of the microporous phase, with a value of 57 m^{-1} (17.4 ft^{-1}).

The major results for samples A, F, K, and N are summarized in Table 2.

DISCUSSION

Electrical Resistivity to Porosity Relationship

The three studied zones are all characterized by a strong reduction of porosity caused by a highly indurated phase but present different porosity types: the porosity at MC10-61 and MC11-37 is mostly intergranular, with few vugs found in the case of MC11-37. The porosity at MC10-25 displays many more vugs. The formation factor is higher for that zone, which is in good agreement with the results of Verwer et al. (2011), and so is the cementation

index, with the highest values of m found for the most vug-rich samples, as suggested by Focke and Munn (1987). The tight part of the three zones consists of a well-cemented matrix, and the more porous part contains many dissolved bioclasts. In the tightest parts, the rock is almost crystalline with very few pores that are likely to be not connected. Because this type of separated porosity would have only a small contribution to the measured resistivity, an increase of this porosity would not have a significant impact on the electrical properties. This might explain the fact that, for the tight samples, when porosity decreases, F does not increase much.

The data confirm that porosity alone is not sufficient to explain electrical measurements in carbonates. They also show that the classical pore-type classifications such as given by Choquette and Pray (1970) and Lucia (1995) might present some correlations with the electrical data but are also not sufficient because samples with similar porosity values and pore type can have significantly different electrical properties. Furthermore, in such heterogeneous carbonate rocks, distinct pore types can be found at the same depth, which prevents

differentiating one sample from another using porosity type considerations only. Other parameters such as the geometry and the topology of the pore space are then needed to better characterize the structure. Therefore, we investigated the 3-D microstructure of the measured samples using XRMT images. In most studies of the petrophysical properties of carbonates and their link with the structure, the pore structure was investigated through the observation and the digital image analysis of thin sections, but they are 2-D representations of the pore structure. Although they may be convenient for evaluating the geometry of the pores and grains, they cannot be used for assessing the real pore-throat arrangement and, more importantly, the connectivity of the pore network, which is the major factor controlling fluid flow and transport in the porous media (Nimmo, 2004; Casteleyn et al., 2010).

Characterization of the Pore Network by X-Ray Microtomography

Within MC10-25, some samples present different values of F , and so m and τ_{mes} for a given porosity ($\sim 15\%$). The XRMT images clearly identify two zones with a different pore structure, corresponding to the two zones having different petrophysical properties.

The top part (around sample A) corresponds to a solid rock matrix containing only macropores consisting of large dissolution vugs. Some of them are isolated from the pore network formed by the connected ones. The proportion of dead zones is high, and a small subsample is not representative of the connected porous network because it is located in some parts of the sample. The bottom part (around sample N) differs significantly from the top part, with a highly microporous matrix, some cemented elements, and many macropores consisting mostly of vugs and dissolved bioclasts. The observation of XRMT 2-D images (cross section) of sample N, or of a thin section taken at this depth, reveals many macropores (Figure 5). Also, given the high porosity of the sample, one would think that this macroporosity phase forms a connected network. However, the cluster calculation shows that

these macropores are only connected by the microporosity. The mercury injection tests indicate that the mean pore entry effective for the percolation of a nonwetting fluid is smaller than what we defined as macropores (Figure 6). This confirms that microporosity controls the connectivity of the pore space and, so, the permeability of the sample. The total resulting connected pore network in sample N has a much lower proportion of immobile zones and is quite homogeneous: a small subsample is representative of the sample (Table 1). For both samples, the value of the computed connected porosity is in good agreement with the value of porosity measured in the laboratory with the triple weight method and the mercury intrusion porosimetry (Table 2). In the case of samples F and K, no or few percolation clusters were found, whereas porosity measurements tell us that the sample contains some nonnegligible accessible porosity. The pores visible at the resolution of $5.06\ \mu\text{m}$ are probably connected by microporous clusters with a pore size lower than $5.06\ \mu\text{m}$. These samples cannot be segmented properly at this scale: whereas the segmented macroporosity is surely correct, as for samples A and N, the segmented microporosity cannot be because a part of the phase is not visible at this scale. These combined results show that XRMT image analysis can be very effective in the determination of the porosity of a porous media and its connectivity, providing that the smallest pores involved in the studied processes have a size bigger than the resolution of the XRMT images. The presence of micropores smaller than $5\ \mu\text{m}$ can be confirmed on the XRMT images of smaller samples allowing higher resolution. For example, a resolution of $0.42\ \mu\text{m}$ can be reached with samples of 2-mm diameter. Scanning electron microscope observation of thin sections can also be used for qualitative appraisal of the microporosity structure, but the 2-D nature of this imaging technique prevents any quantitative appraisal.

For samples A and N, the electrical tortuosity computed from the XRMT images is similar to the one calculated from the measured porosity and formation factor, when the immobile zones are included in the pore network. The result is more

obvious for sample A because it contains more immobile zones. When calculated on the connected pore network after removing the immobile domain, the tortuosity is much lower. Katsube et al. (1991) attempted to remove the effects of pocket porosity, which they define as dead-end pore space and enlargements along the flow path, and proposed a formula to calculate a true tortuosity giving much lower values of tortuosity that they considered as a better measure of the actual sinuosity of the pore channels traversing the rocks. Morphological parameters are also effectively calculated from the XRMT images. Note that the 3-D aspect of these methods is again of great importance when it comes to pore geometry characterization. When working with fewer than three dimensions, one does not know what part of the pore the selected slice intersects (Nimmo, 2004). Coker and Torquato (1995) especially insisted on the intrinsically 3-D nature of the pore-size distribution measure because it reflects connectedness information about the spherical regions of a given radii, which could not be obtained from plane measurements such as thin-section image analysis.

Influence of the Pore Structure on Petrophysical and Flow Properties

Now, let us compare two samples from the two different zones presenting a similar order of magnitude of porosity: sample A ($\phi_{\text{exp}} = 14.9\%$) and sample J ($\phi_{\text{exp}} = 14.4\%$). Sample A belongs to the top zone, which contains large simple pores, whereas sample J, located close to sample K, is in the bottom part, characterized by macropores connected to the network only by a small intricate microporosity network (smaller pore size and higher specific surface). Sample A presents higher values of formation factor ($F = 183$), cementation index ($m = 2.74$), and electrical tortuosity ($\tau_{\text{mes}} = 5.23$) than sample J ($F = 110$, $m = 2.42$, and $\tau_{\text{mes}} = 3.98$). These results suggest that higher values of electrical resistivity are expected for a pore space having larger pores and a smaller specific surface suggesting a simple network, compared with a complicated pore system dominated by micropores. These results derived from the analysis of

3-D images confirm the work of Verwer et al. (2011), who quantified the pore structure in 2-D.

The difference of the pore systems between the two zones is even more visible on the permeability, which is approximately four orders of magnitude smaller for J ($k \approx 0.008$ md) than for A ($k \approx 80$ md). The major difference between the two samples is the size of the pore diameter connecting the pore network, which appears to seriously limit the flow of fluid, as previously reported (Kozeny, 1927; Carman, 1937; Gouze and Luquot, 2011). The formation factor and the tortuosity are commonly used as a measure of flow efficiency, and the Kozeny-Carman equations incorporating these parameters suggest a decrease in the permeability with an increase in resistivity and tortuosity. The opposite is found here: sample A is much more permeable, although it is more resistive and tortuous. These results show that the electrical flow is more efficient in a dense pore network characterized by a high number of pores, even if they are small, whereas the hydraulic flow is highly controlled by the size of the pores and will be more efficient when the size of the diameter of the effective hydraulic path is larger. Therefore, samples with high resistivity can have a high permeability. This data set highlights the differences between the electrical and hydraulic pathways reported in Clennell (1997).

The comparison between samples F and K confirms the high control of the hydraulic diameter on the permeability: although sample K has a much higher value of porosity than sample F, its permeability is not much higher. Because of its extremely low pore size, the microporosity seems not very effective for controlling the flow properties. In addition, sample N, which is the most porous and least resistive and tortuous sample of the data set, is not the most permeable because the macropores are still connected by micropores.

Different modifications of Kozeny-Carman's empirical equations were tried out to estimate the permeability from the porosity by incorporating the pore geometry parameters that can be assessed from processing XRMT images (specific surface, pore size of the connected network) or measured on cores (formation factor, electrical tortuosity, mean pore

throat). For instance, Walsh and Brace (1984) proposed the following formulation:

$$k = \frac{\phi^2}{2 \times F \times \left(\frac{S}{V}\right)^2} \quad (9)$$

This equation relating the permeability to the porosity, the specific surface, and the formation factor (or the tortuosity) was reported successfully by Blair et al. (1996). In our case, equation 9 failed to predict the values of permeability measured on cores. We tested several similar equations found in the literature, but all failed to be applicable to the studied rocks. Keep in mind that all these relations are generally derived, assuming some simple structures of the pore space, and incorporate some of the parameters controlling the permeability but not all. Because the flow properties of a rock depend on many interconnected parameters, it is obviously impossible to summarize all of these interactions in one simple equation, especially for media presenting a wide range of pore sizes and shapes such as carbonate rocks. Yet, the relation (equation 10) proposed by Thompson et al. (1987) fits remarkably well the results:

$$k = \left(\frac{1}{226}\right) \times \frac{d_c^2}{F} \quad (10)$$

where d_c , named the “critical pore size” by Thompson et al. (1987), is the size of the smallest pore invaded by a nonwetting phase at breakthrough conditions and is equivalent to d_{Hg} . The size of the pore throats that are connecting the pore space seems then to be the most important factor controlling the permeability in carbonate rocks.

CONCLUSION

Because of the complexity and variability of their pore network, carbonate rocks of similar porosity may display a wide range of electrical resistivity and permeability. The influence of the pore structure on these properties and, in particular, on the relationships between resistivity and porosity as well as permeability and porosity, should then be studied in detail.

Therefore, the pore space morphology including, for instance, the spatial organization between the different types of pores and throats needs to be characterized.

The investigation of centimeter-scale heterogeneities requires 3-D images having a field of view of at least a few centimeters and a resolution on the order of a few micrometers. In the study, we used XRMT images and proposed specific data processing tools that can be used for extracting a set of relevant parameters that quantify the pore size and shape and the architecture of the pore network including its connectivity and tortuosity.

- This methodology improves significantly the ability to perform the necessary multiscale characterization of the 3-D pore structure, and because the XRMT methods are nondestructive, the corresponding petrophysical measurements can be conducted on the exact same sample.
- We achieved the determination of the connectivity of the macroporosity, and we also identified the presence of microporous cements and their function in assuring the connectivity between the nonconnected macropores.
- Once the connected pore network was properly estimated, the electrical tortuosity was effectively computed in a very short time compared to the measurements in the laboratory, which requires at least three or four measurements at different salinities.
- Microstructural descriptors such as the pore-size distribution function and the specific surface were efficiently computed from the XRMT images and gave valuable insight into the size and shape of the connected network, which are the major factors controlling permeability.

The reefal carbonate layers studied display large changes in porosity and, consequently, in their petrophysical properties at centimeter scale. The data showed the following:

- In general, the formation factor increases when porosity decreases, but large variations are observed.
- The tightest samples strongly deviate from Archie’s equation, presenting a lower resistivity

than expected. The electrical resistivity is higher for the vug-rich samples (MC10-25), which also display higher values of the cementation index ($m > 2$).

The detailed analysis of the pore structure of one zone (MC10-25) using XRMT images confirmed the following:

- Samples with large simple pores (high pore size and low specific surface), such as vugs or molds, have high values of resistivity, cementation factor, and electrical tortuosity, and inversely, samples characterized by a complex network with small pores (small pore size and high specific surface) have low values of resistivity, velocity, cementation factor, and electrical tortuosity.
- Contrary to what could have been conjectured from the standard relationship, the most porous and least resistive sample (sample N) is not the most permeable, and a much less porous and more resistive sample (sample A) can be more permeable. This example illustrates that hydrodynamic flow strongly depends on the critical pore size (very small in sample N) and greatly differs from electrical conduction.

This study highlights the remarkable millimeter-scale heterogeneity of the studied carbonate data set and its control on the macroscopic petrophysical and hydrodynamical properties. In reservoir engineering, porosity, water saturation, and permeability are commonly estimated from electrical data using heuristic resistivity-porosity and porosity-permeability relationships that have been proven to be successful in sandstones. However, we have shown here that one cannot rely on these relationships in carbonate rocks, precisely because of the combination of two realities: first, heterogeneities occur at scales smaller than those of the integration volume of the borehole geophysical methods (tens to hundreds of cubic centimeters in the best cases), and second, these micrometer- to centimeter-scale heterogeneities strongly influence the measured macroscopic physical parameters that are then used to evaluate the hydrodynamic properties

of the rock. For application to such highly heterogeneous carbonates, we believe that borehole geophysical measurements should be associated with both multiscale imagery techniques and core-scale geophysical properties measurements.

REFERENCES CITED

- Archie, G. E., 1942, The electrical resistivity log as an aid in determining some reservoir characteristics: *Journal of Petroleum Technology*, v. 5, p. 1–8.
- Bear, J., 1972, *Dynamics of fluids in porous media*: New York, American Elsevier, 166 p.
- Blair, S. C., P. A. Berge, and J. G. Berryman, 1996, Using two-point correlation functions to characterize microgeometry and estimate permeabilities of sandstones and porous glass: *Journal of Geophysical Research*, v. 101, p. 20,359–20,375, doi:10.1029/96JB00879.
- Carman, P. C., 1937, Fluid flow through granular beds: *Transactions of the Institution of Chemical Engineers*, v. 15, p. 150–166.
- Carman, P. C., 1956, *Flow of gases through porous media*: London, United Kingdom, Butterworths, 182 p.
- Casteleyn, L., P. Robion, C. David, P. Y. Collin, B. Menéndez, N. Fernandes, G. Desaubliaux, and C. Rigollet, 2010, An integrated study of the petrophysical properties of carbonate rocks from the “Oolithe Blanche” formation in the Paris Basin: *Tectonophysics*, v. 503, p. 18–33, doi:10.1016/j.tecto.2010.09.031.
- Chilingarian, G. V., S. J. Mazzullo, and H. H. Rieke, 1992, *Carbonate reservoir characterization: A geologic-engineering analysis, Part I*: Amsterdam, Netherlands, Elsevier Science, *Developments in Petroleum Science*, v. 30, 640 p.
- Choquette, P. W., and L. C. Pray, 1970, Geologic nomenclature and classification of porosity in sedimentary carbonates: *AAPG Bulletin*, v. 54, p. 207–244.
- Clennell, B., 1997, Tortuosity: A guide through the maze, in M. A. Lovell and P. K. Harvey, eds., *Developments in petrophysics*: Geological Society Special Publication 122, p. 299–344.
- Coker, D. A., and S. Torquato, 1995, Extraction of morphological quantities from a digitized medium: *Journal of Applied Physics*, v. 77, p. 6087–6099, doi:10.1063/1.359134.
- Cornell, D., and D. L. Katz, 1953, Flow of gases through consolidated porous media: *Industrial and Engineering Chemistry*, v. 45, p. 2145–2152, doi:10.1021/ie50526a021.
- Dentz, M., P. Gouze, A. Russian, J. Dweik, and F. Delay, 2012, Diffusion and trapping in heterogeneous media: An inhomogeneous continuous time random walk approach: *Advances in Water Resources*, v. 49, p. 13–22, doi:10.1016/j.advwatres.2012.07.015.
- Dullien, F. A. L., 1979, *Porous media: Fluid transport and pore structure*: New York, Academic Press, 396 p.
- Esteban, M., 1979, Significance of the upper Miocene reefs in the western Mediterranean: *Palaeogeography, Palaeoclimatology,*

- Palaeoecology, v. 29, p. 169–188, doi:[10.1016/0031-0182\(79\)90080-4](https://doi.org/10.1016/0031-0182(79)90080-4).
- Focke, J. W., and D. Munn, 1987, Cementation exponents in Middle Eastern carbonate reservoirs: Society of Petroleum Engineers Formation Evaluation, v. 2, p. 155–167.
- Garing, C., 2011, Caractérisation géophysique et géochimique des interactions fluide-roche à l'interface eau douce-eau salée: Cas des carbonates récifaux de Majorque: Ph.D. thesis, University of Montpellier 2, Montpellier, France, 244 p.
- Gouze, P., and L. Luquot, 2011, X-ray microtomography characterization of porosity, permeability and reactive surface changes during dissolution: Journal of Contaminant Hydrology, v. 120–121, p. 45–55.
- Gouze, P., Y. Melean, T. Le Borgne, M. Dentz, and J. Carrera, 2008, Non-Fickian dispersion in porous media explained by heterogeneous microscale matrix diffusion: Water Resources Research, v. 44, p. W11416, doi:[10.1029/2007WR006690](https://doi.org/10.1029/2007WR006690).
- Hebert, V., 2011, Analyses multi-échelles de la structure d'un réservoir carbonaté littoral: Exemple de la plate-forme de Llucmajor (Majorque, Espagne): Ph.D. thesis, University of Montpellier 2, Montpellier, France, 302 p.
- Jaeggi, D., 2006, Multiscalar porosity structure of a Miocene reefal carbonate complex: Ph.D. thesis, Eidgenössische Technische Hochschule Zurich, Zurich, Switzerland, 200 p.
- Katsube, T. J., B. S. Mudford, and M. E. Best, 1991, Petrophysical characteristics of shales from the Scotian Shelf: Geophysics, v. 56, p. 1681–1689, doi:[10.1190/1.1442980](https://doi.org/10.1190/1.1442980).
- Kozeny, J., 1927, Über kapillare leitung des wassers im boden: Sitzungsberichte der Akademie der Wissenschaften in Wien, v. 136, p. 127–306.
- Lucia, F. J., 1995, Rock-fabric/petrophysical classification of carbonate pore space for reservoir characterization: AAPG Bulletin, v. 79, p. 1275–1300.
- Luquot, L., and P. Gouze, 2009, Experimental determination and permeability changes induced by injection of CO₂ into carbonate rocks: Chemical Geology, v. 265, p. 148–159, doi:[10.1016/j.chemgeo.2009.03.028](https://doi.org/10.1016/j.chemgeo.2009.03.028).
- Maria Sube, Y., 2008, Structure et hétérogénéité d'une plate-forme récifale Miocène (Majorque): Implication pour les intrusions d'eau salée en zone côtière: Ph.D. thesis, University of Montpellier 2, Montpellier, France, 309 p.
- Mecke, K. R., 2000, Additivity, convexity, and beyond: Applications of Minkowski functionals in statistical physics: Lecture Notes in Physics, v. 554, p. 111–184.
- Meijster, A., J. B. T. M. Roerdink, and W. H. Hesselink, 2000, A general algorithm for computing distance transforms in linear time: Mathematical Morphology and Its Application to Image and Signal Processing, Computational Imaging and Vision, v. 18, no. 8, p. 331–340.
- Michielsen, K., and H. De Raedt, 2001, Integral-geometry morphological image analysis: Physics Reports, v. 347, p. 461–538, doi:[10.1016/S0370-1573\(00\)00106-X](https://doi.org/10.1016/S0370-1573(00)00106-X).
- Moore, C. H., 2001, Carbonate reservoirs, porosity evolution and diagenesis in a sequence-stratigraphic framework: Oxford, United Kingdom, Elsevier, Developments in Sedimentology 55, 444 p.
- Myroie, J. E., and J. L. Carew, 2003, Karst development on carbonate islands: Speleogenesis and Evolution of Karst Aquifers, v. 1, no. 1, 21 p.
- Nimmo, J. R., 2004, Porosity and pore size distribution, in D. Hillel, ed., Encyclopedia of soils in the environment: London, United Kingdom, Elsevier, v. 3, p. 295–303.
- Noiriel, C., D. Bernard, P. Gouze, and X. Thibault, 2005, Hydraulic properties and microgeometry evolution accompanying limestone dissolution by acidic water: Oil & Gas Science and Technology, v. 60, p. 177–192, doi:[10.2516/ogst.2005011](https://doi.org/10.2516/ogst.2005011).
- Pomar, L., and W. C. Ward, 1999, Reservoir-scale heterogeneity in depositional packages and diagenetic patterns on a reef-rimmed platform, upper Miocene, Mallorca, Spain: AAPG Bulletin, v. 83, no. 11, p. 1759–1773.
- Pomar, L., W. C. Ward, and D. G. Green, 1996, Upper Miocene reef complex of the Llucmajor area, Mallorca, Spain: SEPM Concepts in Sedimentology and Paleontology, v. 5, p. 191–225.
- Salem, H. S., and G. V. Chilingarian, 1999, The cementation factor for Archie's equation for shaly sandstone reservoirs: Journal of Petroleum Science and Engineering, v. 23, p. 83–93, doi:[10.1016/S0920-4105\(99\)00009-1](https://doi.org/10.1016/S0920-4105(99)00009-1).
- Schlumberger, 1972, Log interpretation: Principles: New York, Schlumberger Limited, v. 1, 113 p.
- Schlumberger, 1974, Log interpretation: Applications: New York, Schlumberger Limited, v. 2, 116 p.
- Stauffer, D., and A. Aharony, 1994, Introduction to percolation theory: London, United Kingdom, Taylor and Francis, 192 p.
- Sundberg, K., 1932, Effects of impregnating waters on electrical conductivity of soils and rocks: Transactions of the American Institute of Mining and Metallurgical Engineers, v. 97, p. 367–391.
- Thompson, A. H., A. J. Katz, and C. E. Krohn, 1987, The microgeometry and transport properties of sedimentary rock: Advances in Physics, v. 36, no. 5, p. 625–694, doi:[10.1080/00018738700101062](https://doi.org/10.1080/00018738700101062).
- Valdés-Parada, F. J., M. L. Porter, and B. D. Wood, 2010, The role of tortuosity in upscaling: Transport in Porous Media, v. 88, p. 1–30, doi:[10.1007/s11242-010-9613-9](https://doi.org/10.1007/s11242-010-9613-9).
- Verwer, K., G. P. Eberli, and R. J. Weger, 2011, Effects of pore structure on electrical resistivity in carbonates: AAPG Bulletin, v. 95, no. 2, p. 175–190, doi:[10.1306/06301010047](https://doi.org/10.1306/06301010047).
- Vogel, H. J., U. Weller, and S. Schlüter, 2010, Quantification of soil structure based on Minkowski functions: Computers and Geosciences, v. 36, p. 1236–1245, doi:[10.1016/j.cageo.2010.03.007](https://doi.org/10.1016/j.cageo.2010.03.007).
- Walsh, J. B., and W. F. Brace, 1984, Effect of pressure on porosity and the transport properties of rock: Journal of Geophysical Research, v. 89, p. 9425–9431, doi:[10.1029/JB089iB11p09425](https://doi.org/10.1029/JB089iB11p09425).
- Winsauer, W. O., H. M. Shearing, P. H. Masson, and M. Williams, 1952, Resistivity of brine-saturated sands in relation to pore geometry: AAPG Bulletin, v. 36, p. 253–277.
- Wyllie, M. R. J., and W. D. Rose, 1950, Some theoretical considerations related to quantitative evaluation of the physical evaluation of the physical characteristics of reservoir rocks from electric log data: Journal of Petroleum Technology, v. 2, p. 105–118.